Distinct magneto-Raman signatures of spin-flip phase transitions in CrI$_3$

Amber McCreary,[1] Thuc T. Mai,[1,2] Franz G. Utermohlen,[2] Jeffrey R. Simpson,[1,3] Kevin F. Garrity,[4] Xiaozhou Feng,[2] Dmitry Shcherbakov,[2] Yanglin Zhu,[5] Jin Hu,[6] Daniel Weber,[7,⊥] Kenji Watanabe,[8] Takashi Taniguchi,[8] Joshua E. Goldberger,[7] Zhiqiang Mao,[5] Chun Ning Lau,[2] Yuanming Lu,[2] Nandini Trivedi,[2] Rolando Valdés Aguilar,[2,§] and Angela R. Hight Walker[1,]*

[1]Nanoscale Device Characterization Division, Physical Measurement Laboratory, National Institute of Standards and Technology, Gaithersburg, Maryland 20899, USA
[2]Department of Physics, The Ohio State University, Columbus, OH 43210, USA
[3]Department of Physics, Astronomy, and Geosciences, Towson University, Towson, MD 21252, USA
[4]Materials Measurement Science Division, Material Measurement Laboratory, National Institute of Standards and Technology, Gaithersburg, Maryland 20899, USA
[5]Department of Physics, The Pennsylvania State University, University Park, PA 16802, USA
[6]Department of Physics, University of Arkansas, Fayetteville, AR 72701, USA
[7]Department of Chemistry and Biochemistry, The Ohio State University, Columbus, OH 43210, USA
[8]National Institute for Materials Science, 1-1 Namiki Tsukuba Ibaraki 305-0044, Japan
[⊥]Current address: Battery and Electrochemistry Laboratory, Institute of Nanotechnology, Karlsruhe Institute of Technology, 76344 Eggenstein-Leopoldshafen, Germany

*Email: angela.hightwalker@nist.gov

§Email: valdesaguilar.1@osu.edu

ABSTRACT: The discovery of 2-dimensional (2D) materials, such as CrI_3, that retain magnetic ordering at monolayer thickness has resulted in a surge of both pure and applied research in 2D magnetism. Here, we report a magneto-Raman spectroscopy study on multilayered CrI_3, focusing on two new features in the spectra that appear below the magnetic ordering temperature and were previously assigned to high frequency magnons. Instead, we conclude these modes are actually zone-folded phonons. We observe a striking evolution of the Raman spectra with increasing magnetic field applied perpendicular to the atomic layers in which clear, sudden changes in intensities of the modes are attributed to the interlayer ordering changing from antiferromagnetic to ferromagnetic at a critical magnetic field. Our work highlights the sensitivity of the Raman modes to weak interlayer spin ordering in CrI_3.

Magnetic van der Waals-bonded materials represent a rapidly growing research field,[1-6] where these materials provide a solid-state platform to study a variety of exciting physics and potential applications of magnetism in two dimensions, including proximity effects, control using strain and gating, spin fluctuations, magnetic excitations, spintronics, and possible quantum spin liquids.[7] One material of particular interest is chromium tri-iodide (CrI_3), a ferromagnet (FM) at bulk thicknesses below the Curie temperature (T_c) but with the remarkable property of layered antiferromagnetism (AFM) in thin multilayers.[2] While each individual layer is FM, the layers themselves are AFM coupled, and this effect persists for samples tens of layers thick. Furthermore, the interlayer spin arrangement in CrI_3 can be switched between AFM and FM by an electric field,[8-10] applied pressure,[11] and a magnetic field,[2,12-15] providing tunability in potential devices.

Raman spectroscopy is a powerful technique to study a variety of phenomena in 2D quantum materials, including effects of strain,[16] electron-phonon coupling,[17] phase transitions,[18] spin-phonon coupling,[19] and magnetic excitations.[20-22] Additionally, the diffraction-limited spot size allows for the investigation of atomically thin samples and heterostructures using a non-contact probe. In this work, we collect temperature- and magnetic field (B)-dependent Raman spectra on a thin (~10 layers) CrI_3 single crystal encapsulated in hexagonal boron nitride (hBN). Interestingly, at low temperature, increasing the magnetic field results in dramatic changes in the Raman spectra, indicating a magnetic field-induced phase transition when the interlayer spin

arrangement changes from AFM to FM. By calculating the phonon dispersion of CrI_3 in both the FM and AFM state, we conclude that the new modes appearing in the AFM state are zone-folded phonons. This work validates magneto-Raman spectroscopy as a sensitive technique to probe interlayer magnetic ordering in quantum materials.

A thin flake of CrI_3 ($\approx$7 nm from atomic force microscopy, or $\approx$10 layers) was encapsulated between two 20 nm to 30 nm flakes of hBN using the dry transfer technique.[22,23] In the *ab* plane, the Cr^{3+} atoms are arranged in a honeycomb lattice, where each Cr atom is bonded with six I atoms to form a distorted octahedron (see Figure 1a and Figure S1). At room temperature, bulk CrI_3 has a monoclinic structure (C2/m) but exhibits a crystallographic phase transition near 220 K to rhombohedral ($R\overline{3}$),[25] where the main difference between the two structures is the stacking of the layers (see Figure S1). The bulk T_c is around 61 K,[25] with the spins aligned perpendicular to the *ab* plane. Surprisingly, the magnetic behavior of thinner samples is very different; while the spins still align perpendicular to the *ab* plane, the interlayer magnetic stacking is AFM, as demonstrated through a variety of experimental techniques.[2,8,9,12-15,26,27] It has been theoretically[28-31] and experimentally[27,31] suggested that atomically thin CrI_3 does not go through the crystallographic phase transition that the bulk does, but instead remains in the monoclinic structure at low temperatures, resulting in AFM interlayer stacking.

Raman spectra were collected with a triple grating spectrometer using an excitation laser wavelength of 632.8 nm and keeping the power below 150 μW ($\approx$1 μm spot size) at the sample to avoid heating. The laser polarization of the incoming ε_i light makes an angle φ with respect to the *b* axis (Figure 1a), and the scattered ε_s light angle θ is changed from θ = 0° (parallel, *xx*) to θ = 90° (perpendicular, *xy)*. Since the crystallographic *a* and *b* axes are not known in our sample, the angle φ is an arbitrary, yet constant, angle in our experiments. Figure 1b shows the Raman spectra at *T* = 5 K, in both the *xx* and *xy* configurations. We confirm the monoclinic symmetry in our $\approx$10 layer flake by resolving two peaks at 108 cm^{-1} and 109 cm^{-1} between *xx* (black, scaled by 0.5) and *xy* (red), unlike the doubly-degenerate peak seen in the rhombohedral structure.[32] Thus, we label the phonons using the irreducible representations of the 2/m point group, where only the A_g and B_g modes are Raman active.[33,34] The density functional theory (DFT) calculated atomic displacements associated with these modes are shown in the Supplemental Information.

Two new modes appear below T_c in the *xy* configuration at 77 cm^{-1} (9.5 meV) and 126 cm^{-1} (15.6 meV), labeled P_1 and P_2 in Figure 1b, respectively. These modes were previously attributed to magnon excitations since they appear in the magnetically ordered state and have their largest intensity in *xy* (inset of Figure 1b), indicating B_g symmetry.[35] Instead, the bulk magnon dispersion[36] at 5 K shows a low-energy magnon at Γ below 1 meV (8 cm^{-1}), similar to what was measured by recent FM resonance (FMR) experiments,[37] and magnons at the M point of the Brillouin zone at ~9 meV and 15 meV. Furthermore, a recent Raman study of magnon excitations in FePS$_3$ showed it is possible for magnons to be present in both *xx* and *xy* in quasi-2D van der Waals magnets.[20] Thus, the B_g nature of P_1 and P_2 is not conclusive evidence that they are magnons.

We studied the effects of an applied magnetic field on P_1 and P_2, as detailed in Figure 2. Two spectral ranges from 65 cm^{-1} to 90 cm^{-1} (P_1, A_g^1) and 120 cm^{-1} to 136 cm^{-1} (P_2, A_g^6) are shown on different intensity scales ($\approx$ a factor of 3 to 1, respectively) for clarity. At $B = 0$ T and in *xy*, P_1 and P_2 have strong intensities, whereas the two A_g modes at slightly higher frequencies have minimum intensities as they are forbidden in the *xy* configuration. Increasing the magnetic field results in drastic changes in the Raman spectra, where P_1 and P_2 behave in the same fashion. Above $\approx$1.6 T, the intensities of P_1 and P_2 abruptly start to vanish and A_g^1 and A_g^6 begin to appear in *xy*. By $B = 2$ T, P_1 and P_2 are absent in all polarization configurations, while A_g^1 and A_g^6 are no longer forbidden in *xy*. No further changes occur above 2 T, and no hysteresis was observed when the field was lowered back to 0 T. It should be noted that P_1 and P_2 do not show frequency shifting with magnetic field, suggesting they are not one-magnon processes with spins perpendicular to *ab*.

Raman spectra were collected as the magnetic field was increased in finer steps up to 2 T. This is shown as a false-color map (Figure 3a) and spectra (Figure 3b) for the frequencies near P_2 and A_g^6, where six distinct magnetic field ranges are revealed. Upon close inspection, there is additional Raman scattering intensity, *i.e.,* spectral weight, present between P_2 and A_g^6 around 128 cm^{-1}, although it cannot be discerned if the spectral weight is attributed to a single or multiple mode(s). No changes to P_2, A_g^6, or the spectral weight in-between were observed in Range 1 from 0 T and 0.6 T. In Range 2 between 0.7 T and 0.8 T, the spectral weight between

them P_2 and A_g^6 appears to shift in frequency and intensity. The spectra are again stable through Region 3 from 0.8 T to 1.4 T, after which striking changes are seen in Regions 4 and 5. In Region 4, P_2 starts to decrease in intensity, the intensity of A_g^6 stays relatively constant, and the spectral weight in-between shifts in frequency and increases in intensity. In Region 5, P_2 and the spectral weight in-between both decrease in intensity until they disappear, while A_g^6 grows in intensity until $B > 1.95$ T (Region 6), when the phase transition is finally complete. It should be noted that experimental uncertainty, including instrument drift and corrections for Faraday rotation in magneto-cryostat objective lenses, can lead to small changes in peak intensities (generally less than 5%) when comparing consecutively taken Raman spectra. The intensity changes being tracked in the field ranges in Figure 3b, however, are more significant than any changes seen in the Γ point phonons (see Figure S3) and are thus outside of experimental uncertainty. Moreover, frequency shifts, such as those observed in the spectral weight between P_2 and A_g^6 in Regions 2 and 4, are significantly more reliable than intensity changes, generally reproducible to within one CCD detector pixel (≈ 0.4 cm^{-1} with HeNe excitation herein). For fitted peaks (*e.g.,* well-defined phonons), the Raman shift frequency is even more precise (better than 0.1 cm^{-1}).

Recent magneto-tunneling measurements of few-layered CrI$_3$ also observed large changes in the tunneling current at nearly the same magnetic field values where we observe dramatic changes in the Raman spectra, such as at 0.8 T and 2 T.[12-15,26] These changes were attributed to the spin-filtering effect when the magnetic field is strong enough to change the interlayer spin arrangement from AFM to FM, and the effect was observed even for 20 nm thick samples (our sample is ≈ 7 nm). The striking resemblance in the evolution with magnetic field observed with magneto-tunneling, including sharp changes between regions of stability, to those reported herein implies Raman spectroscopy is detecting the phase transition caused by layers flipping spins from AFM to FM stacking. The observation of the first jump at 0.8 T in a variety of thicknesses of CrI$_3$ in magneto-tunneling[12-15,26] suggests it is most likely due to the surface layers (adjacent to the hBN) flipping while the second, final jump is the flipping of the internal layers at ≈ 2 T. This spin-flip phase transition is supported by the observation of the lower energy FM magnon for $B > 6.5$ T (Figure S4), which matches previous results on bulk, FM CrI$_3$,[36,37] and the lack of change in the Raman spectra between 2 T and 9 T (Figure S5). The 10 L

sample remains monoclinic at high magnetic fields (Figure S6), demonstrating that a change in crystal structure is not the source of the evolution of the Raman spectra. In particular, the spectral weight present between P_2 and A_g^6 is extremely sensitive to the spin-flipping, displaying strong frequency shifts and intensity variations where the spin flips occur. The fact that the spectral weight does not shift in magnetic field in Regions 1 and 3, which are regions of stability, suggests its presence does not involve a one-magnon process. It is possible that the spectral weight results from the excitation laser wavelength ($\lambda = 632.8$ nm) being nearly resonant with the ligand-to-metal charge transfer transition,[38-41] but the weak Raman signal at off-resonance excitation laser wavelengths makes this difficult to verify.

The polar plots for A_g^6, which track the intensity of A_g^6 as the angle θ (*i.e.*, ε_s relative to ε_i) is changed, at various magnetic fields provide further evidence of the magnetic phase transition. As seen in Figure 4a, the polar plot is rotated by approximately 35° at $B = 2$ T when compared with $B = 0$ T. This can be understood if we write the Raman tensor for the A_g phonon under applied magnetic field ($B \perp ab = B_z$) as:

$$R_{A_g, B \perp ab} = R_{A_g, B=0} + B_z \cdot R_{A_g, B_z} \qquad (1)$$

The point group of CrI$_3$ requires that the total Raman tensor R_{A_g} is symmetric under two-fold rotation around the *b*-axis (C_{2x}). Since B_z itself is antisymmetric under C_{2x}, then the form of R_{A_g, B_z} is required to also be antisymmetric under C_{2x}:

$$R_{A_g, B \perp ab} = \begin{pmatrix} \alpha & 0 \\ 0 & \beta \end{pmatrix} + B_z \begin{pmatrix} 0 & \gamma \\ \delta & 0 \end{pmatrix} \qquad (2)$$

Thus, for the $B = 0$ T case (AFM state), the Raman tensor would be purely symmetric, and we expect to not detect any signal in *xy* polarization configurations. A magnetic field applied perpendicular to the *ab* plane (FM state), however, introduces off-diagonal tensor elements and breaks this expectation, causing the polar plot to rotate as seen in Figure 4a. Assuming there are minimal changes between the monoclinic (C_{2h}), 10 L CrI$_3$ and the hexagonal point group of the monolayer (D_{3d}), then $\beta \approx \alpha + \Delta$ and $\delta \approx -(\gamma + \Delta')$, where Δ and Δ' are small corrections.

$$R_{A_g, +B_z} = \begin{pmatrix} \alpha & B_z \gamma \\ -B_z(\gamma + \Delta') & \alpha + \Delta \end{pmatrix}, \quad R_{A_g, -B_z} = \begin{pmatrix} \alpha & -B_z \gamma \\ B_z(\gamma + \Delta') & \alpha + \Delta \end{pmatrix} \qquad (3)$$

Writing the matrices as in Eq. (3) makes it clearer that when the magnetic field direction is flipped from B_z to $-B_z$, the signs of the off-diagonal elements switch, resulting in the opposite rotation of the polar plot, exactly as we observed in Figure 4b.

Figure 4c shows the angle of maximum intensity of the polar plot in 4a as the magnetic field is swept through the phase transition, where Regions 1-6 from Figure 3 are marked with vertical dashed lines. While Figure 3 and magneto-tunneling results indicate that parts of the phase transition occur between Regions 2 and 4, there is no observable change in the maximum intensity of the polar plot in those field ranges. In Region 5, however, it increases to ≈10° for $B =$ 1.7 T and 1.8 T, and then finally to ≈35° for 1.8 T and above. The fact that the observed change in the angle of maximum intensity of the polar plots is not linear with magnetic field, but instead remains constant until Region 5 indicates that B_z should be regarded as the magnetization of the system induced by an external magnetic field rather than the field itself. The lack of rotation of the polar plot between 0.7 T and 0.8 T reveals that not enough magnetization is induced in this field range to introduce the off-diagonal Raman tensors in Eq. (2).

The temperature dependence of the spin-flips was investigated by tracking the intensity of P_2 as a function of magnetic field for different temperatures between $T = 9$ K and 26 K, as detailed in Figure 4d. The intensity of P_2 is shown relative to the intensity of the combination peak A_g^5/B_g^3 at ≈ 115 cm^{-1} at $B = 0$ T for each temperature, as this peak appears to remain constant with temperature and magnetic field (in the probed range). The spin-flip transition field, or the amount of magnetic field necessary to cause P_2 to disappear, decreases with increasing temperature. In addition, the distinct jumps from spin flips and flat plateaus observed in the intensity of P_2 smooth out for higher T. Further temperature dependence is analyzed in Figure S8. This behavior is consistent with a phase transition where there is a strong correlation between the temperature and magnetic field, which suggests that the magnetic field takes the transition temperature to zero. While this behavior is akin to a quantum phase transition, there is no evidence yet of any quantum critical behavior in this material, but it is a very interesting avenue for future investigation.

Finally, we investigated the directional dependence of the spin-flip phase transition by rotating the sample such that the applied magnetic field is parallel to the ab plane ($B \parallel ab$). Figure 4e shows $I(P_2)/I\left(A_g^5/B_g^3\right)$ for $B \parallel ab$ and at $T = 2$ K. Unlike in the case for $B \perp ab$, no

jumps or plateaus are observed in the intensity of P_2. Instead, the intensity of P_2 continuously decreases with increasing applied field up to $B = 6$ T, after which the layers are stacked FM with the spins pointing in the *ab* plane. This observation matches nicely with measurements of the magneto-tunneling current when the field is in the *ab* plane.[12-15] Furthermore, no frequency shift of P_2 is observed as a function of magnetic field (Figure S10). We perform the same tensor analysis done for Eqs. (1) and (2) above, but this time for the magnetic field applied in the *ab* plane.

$$R_{A_g,B\|ab} = R_{A_g,B=0} + B_x \cdot R_{A_g,B_x} + B_y \cdot R_{A_g,B_y} \tag{4}$$

where x (y) corresponds to *b*-axis (*a*-axis). Requiring that the total Raman tensor be symmetric under C_{2x}, then $R_{A_g,B\|ab}$ is written as:

$$R_{A_g,B\|ab} = R_{A_g,B=0} + B_x \begin{pmatrix} \alpha' & 0 \\ 0 & \beta' \end{pmatrix} + B_y \begin{pmatrix} 0 & \gamma' \\ \delta' & 0 \end{pmatrix} . \tag{5}$$

From Eq. (5), when the magnetic field is directed along the *b*-axis and strong enough to align the spins along the *b*-axis, we expect the Raman tensor to be symmetric and the polar plot of the intensity of A_g^6 as a function of θ not to rotate. However, when the magnetic field has a component pointed along the *a*-axis, off-diagonal tensor elements are introduced, and some rotation of the polar plot would be expected. To test these predictions, we rotated the sample while the magnetic field was applied in the *ab* plane such that the magnetic field was pointed along two different crystal orientations φ_1 and $\varphi_2 = \varphi_1 + 90°$. The polar of the intensity of A_g^6 at $B = 0$ T and 7 T (in the spin-polarized state) are shown in Figure 4f. Interestingly, for both orientations, in which one of them must contain magnetic field components along the *a*-axis, the polar plot of the intensity of A_g^6 does not show the same rotation that was observed for spins pointing perpendicular to the *ab* plane in the spin-polarized state. This indicates that the off-diagonal elements γ' and δ' are negligible for magnetic fields pointing in the *ab* plane.

Our data implies P_1 and P_2, which appear (disappear) in the AFM (FM) state, are not one-magnon excitations, as their frequencies do not shift with applied magnetic field. After considering other theoretical models (see Supplementary Information), we conclude that P_1 and P_2 are actually zone-folded phonons due to a doubling of the AFM unit cell in the *c*-direction. This is illustrated in Figure 5a, where the opposite spins of consecutive layers in the AFM

configuration lead to a unit cell that is twice as large in the c-direction as compared to the FM configuration.

Using DFT, we calculated the phonon dispersions for monoclinic, bulk CrI$_3$ in both the FM and AFM stacking configurations. The full phonon dispersions, Brillouin zone, and table of frequencies are given in Figure S12 and Table S2. Figure 5b shows only the Raman active phonons in the FM state (red, solid) and AFM state (blue, dotted) for frequencies near P_1 and P_2. In general, Raman spectroscopy is only sensitive to modes at the Γ point in the phonon dispersion due to conservation of momentum. Thus, phonons at the A point (in direction of k_z) in the FM state are not observed. However, the doubling of the unit cell in the AFM state leads to zone-folding, where the phonons at the A-point in the Brillouin zone in the FM state fold back onto Γ in the AFM state and can be observed in Raman spectroscopy. Two pairs of modes with similar frequencies to P_1/A_g^1 and P_2/A_g^6 have an easily resolvable frequency splitting at Γ (highlighted Figure 5b), with the zone-folded phonon (P_1 or P_2) between 2 cm^{-1} and 4 cm^{-1} lower in frequency than the original phonon (A_g^1 or A_g^6). Illustrations of these vibrations are shown in Figures 5c and 5d, where the two layers vibrate in-phase for A_g^1 and A_g^6 and out-of-phase for P_1 and P_2. In the bulk, P_{12} would have B_u symmetry and would thus be Raman silent but infrared active. However, the breaking of inversion symmetry for an even number of layers in the AFM configuration would allow P_{12} to be Raman active with B symmetry (only seen in xy configurations). These zone-folded phonons would not shift in magnetic field and would be Raman-active (forbidden) in the AFM (FM) state, aligning with the observed behaviors of P_1 and P_2.

Even though the doubling of the unit cell is purely magnetic in nature, the observation of very strong zone-folded phonons that have similar intensity as the observed Γ point phonons reveals the strong coupling between magnetism and the lattice in atomically thin CrI$_3$. Of note, the origins of P_1 and P_2 as zone-folded phonons predict they would disappear for a monolayer sample (no zone-folding) or a sample with an odd number of layers because the AFM state preserves inversion symmetry with an odd number of layers. Recent work[42,43] has shown P_1 and P_2 are not present in monolayers of CrI$_3$, yet data by Jin et $al.$[35] suggests the presence of P_1 and P_2 for odd layer thicknesses. One possibility is that the encapsulation of thin layers of CrI$_3$ in hBN breaks inversion symmetry naturally, leading to the presence of P_1 and P_2 in all

thicknesses. Further studies as a function of layer thickness and encapsulation parameters are needed to elucidate the symmetry response of P_1 and P_2 for even vs. odd numbers of layers.

In conclusion, we utilized magneto-Raman spectroscopy to elucidate a magnetic phase transition in CrI_3 where the interlayer stacking changes from AFM to FM. Substantial changes in the Raman spectra are detected at specific magnetic field values due to spin-flips of layers to a FM state, indicating that Raman modes are extremely sensitive to this phase transition. Moreover, Raman scattering proves to be crucial to understanding the symmetry and frequency shifts of the modes. We conclude that the new modes P_1 and P_2 are not high frequency magnons as previously believed, but instead attribute the modes to zone-folded phonons using symmetry arguments, polarization-dependent Raman responses, and calculated phonon dispersions in the FM and AFM stacking configurations. This study paves the way for further use of magneto-Raman spectroscopy to investigate spin-flip phase transitions in 2D van der Waals magnets.

METHODS

Sample Preparation and Encapsulation: Bulk CrI_3 crystals were grown by a chemical vapor transport technique using stoichiometric mixtures of Cr and I in a sealed evacuated quartz tube, as mentioned in other references.[25,44] The phase of the obtained crystals were checked by x-ray diffraction. These crystals were then exfoliated onto Si/SiO_2 substrates in an Ar-filled glovebox having O_2 and H_2O concentrations of < 0.1 ppm. $hBN/CrI_3/hBN$ heterostructures were fabricated using a dry transfer technique detailed elsewhere.[23,24] Specifically, PDMS (polydimethylsiloxane) was used as the polymer stamp.

Raman Spectroscopy: Raman spectra were measured with the 632.8601 nm excitation wavelength of a He-Ne laser in the 180° backscattering configuration using a triple grating Raman spectrometer (Horiba JY T64000[†], 1800 mm^{-1} grating) coupled to a liquid nitrogen cooled CCD detector. Polarization was selected and controlled using ultra broadband polarizers and achromatic half wave plates. To perform temperature- and magnetic-field dependent Raman, the sample was placed into an attoDRY cryostat (Attocube Inc.[†]), where the sample holder is pumped to $\approx 1 \times 10^{-3}$ Pa ($\approx 7 \times 10^{-6}$ Torr), backfilled with helium gas, and zero-field cooled. The few-micrometer sized flake of CrI_3 encapsulated in hBN was studied by focusing the laser with a white light camera onto the sample with a low-temperature, magnetic field compatible objective (50×, N.A. 0.82) and xyz nano-positioners. Integration times were approximately 12 minutes and

the laser power was kept below 150 µW to reduce local heating of the sample. Spectra with applied magnetic field were corrected for Faraday rotation in the objective using half wave plates external to the cryostat.

<u>DFT Phonon Calculations</u>: We performed DFT calculations[45,46] with the Quantum Espresso[47] code, using the GBRV ultrasoft pseudopotential set.[48,49] We used the vdw-df-ob86 exchange correlation functional,[50,51] which includes long range van der Waals interactions, for our main results. We also tested the PBEsol[52] functional, finding similar results. Phonon calculations were performed using a finite differences (frozen phonon) approach, using PHONONPY[53] to perform symmetry analysis and the cluster_spring[54] code to calculate phonon dispersions. A 6 x 6 x 4 k-point sampling was used for the ferromagnetic unit cell.

[†]Certain commercial equipment, instruments, or materials are identified in this manuscript in order to specify the experimental procedure adequately. Such identification is not intended to imply recommendation or endorsement by the National Institute of Standards and Technology, nor is it intended to imply that the materials or equipment are necessarily the best available for the purpose.

AUTHOR CONTRIBUTIONS
A.M., T.T.M, J.R.S., R.V.A, and A.R.H.W conceived the project. Bulk CrI_3 crystals were grown by Y.Z, J.H., D.W, J.E.G, and Z.M. Hexagonal boron nitride crystals were supplied by K.W. and T.T. Heterostructures were fabricated by D.S. and C.N.L. Raman measurements and analysis

were carried out by A.M., T.T.M., J.R.S., R.V.A. and A.R.H.W. Theoretical analysis, including modeling and numerical calculations, were carried out by F.U. and X.F., N.T., and Y.-M.L. Phonon DFT calculations were carried out by K.F.G. All authors contributed to the writing of the manuscript.

DATA AVAILABILITY
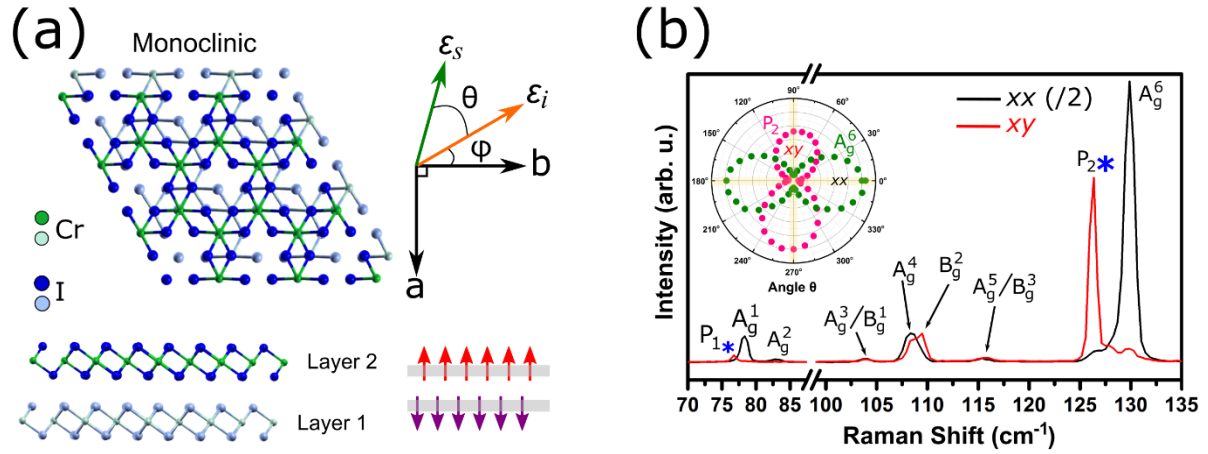
Figure 1: (a) Top and side views of two layers of CrI$_3$ with monoclinic structure and a schematic defining angles θ and φ with respect to the a- and b- crystal axes and the polarization vectors of the incoming ε_i and scattered ε_s light. The two CrI$_3$ layers are color-coded differently. (b) Raman spectra for both xx (black) and xy (red) configurations at $T = 5$ K and $B = 0$ T. Spectra in xx were divided by two for clarity. Inset shows intensity as a function of θ for P_2 and A_g^6 in a polar plot.
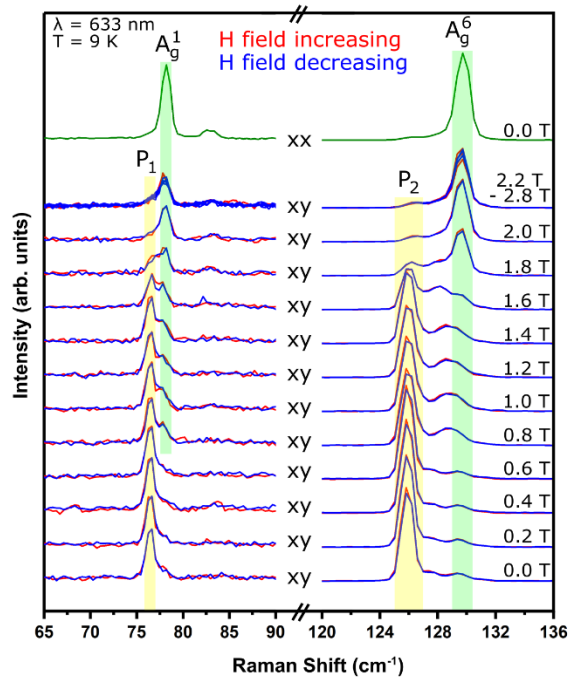
Figure 2: Magnetic field-dependent Raman spectra of CrI_3 from 0 T to 3 T ($B \perp ab$ plane) at $T = 9$ K where P_1 and P_2 disappear above 2.0 T while A_g^1 and A_g^6 appear despite being forbidden in xy configuration. A vertical offset was applied to spectra at different field values. xx spectrum at $B = 0$ T shown at top for comparison.
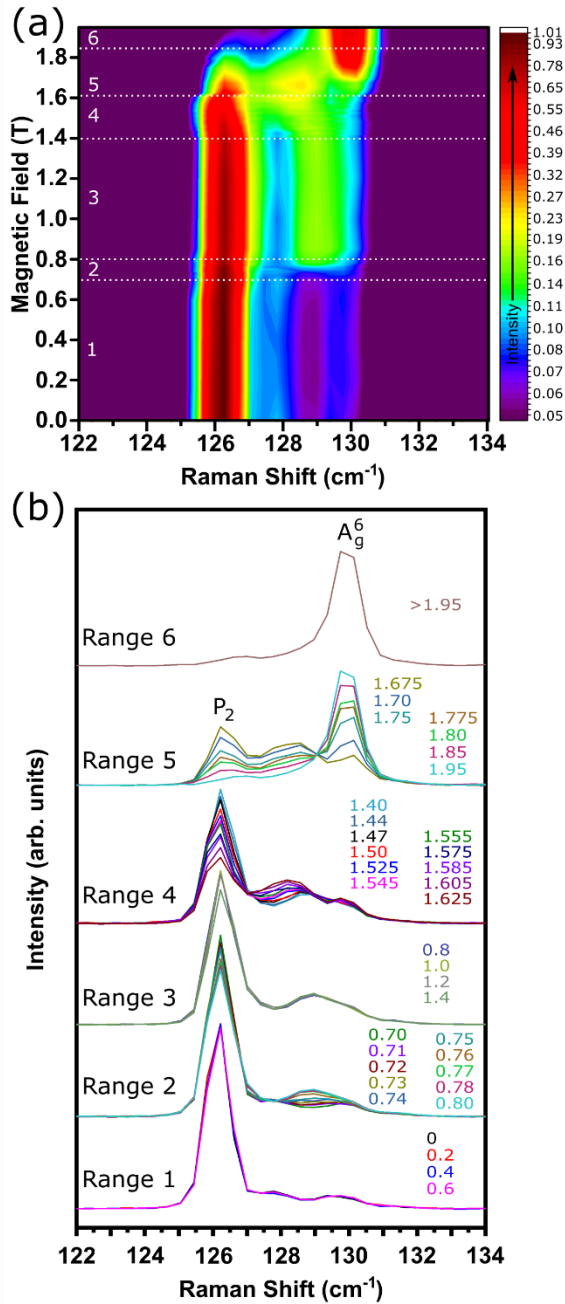
Figure 3: (a) False-color contour map of the Raman intensity (logarithmic) *vs.* magnetic field and shift frequency. (b) Raman spectra at *T* = 9 K, showing a detailed view of the 122 cm^{-1} to 134 cm^{-1} frequency range at different magnetic fields given by legend values (in Tesla). Six distinct field regions are identified below 2 T. A vertical offset was applied to spectra in the different field ranges for clarity.
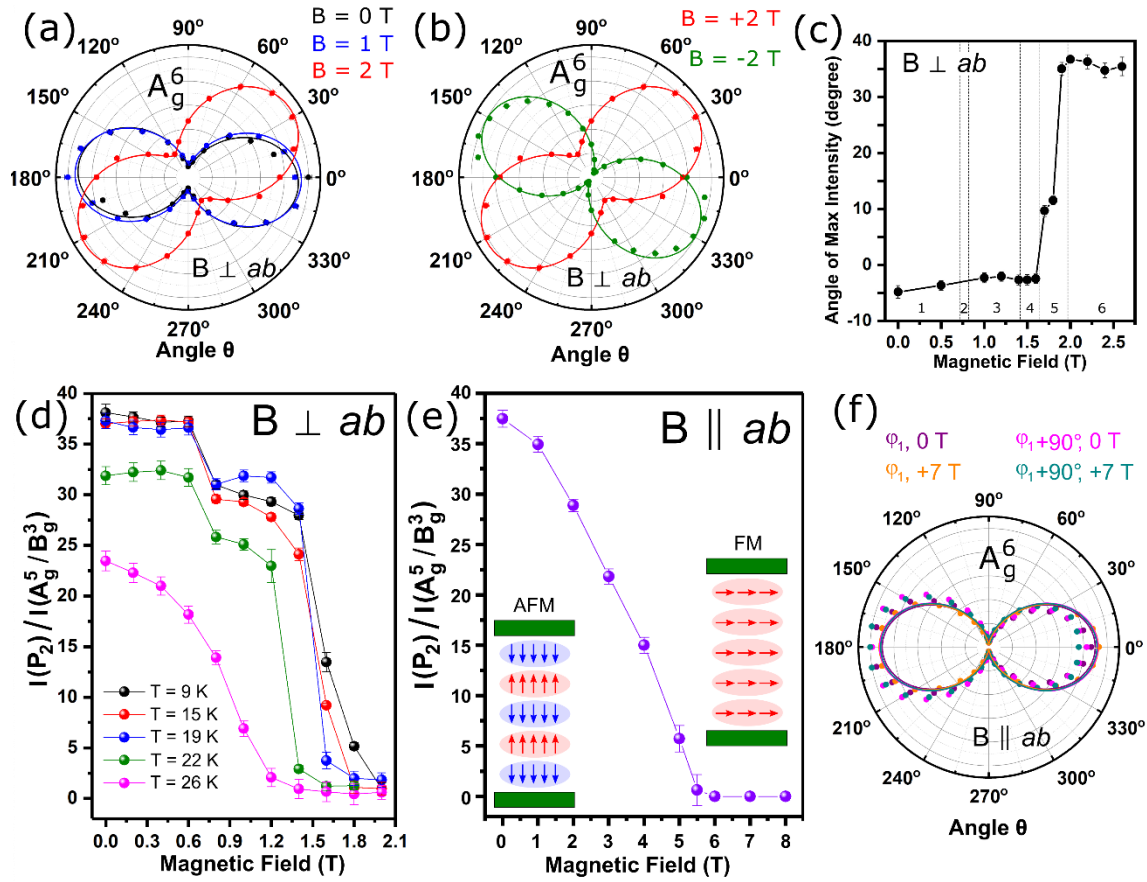
Figure 4: (a) Changes in polar intensity of A_g^6 (maximum intensity normalized to one), as a function of θ for (a) $B = 0$ T, 1 T, and 2 T ($B \perp ab$ plane). (b) Comparing the polar intensity of A_g^6 at positive and negative applied magnetic fields. (c) Angle of maximum intensity in polar plot in (a) as a function of magnetic field, where field ranges from Figure 3(b) are marked. (d) Intensity of P_2 relative to the intensity of the combined mode A_g^5/B_g^3, labeled $I(P_2)/I\left(A_g^5/B_g^3\right)$, as a function of applied magnetic field ($B \perp ab$ plane) at various sample temperatures. (e) $I(P_2)/I\left(A_g^5/B_g^3\right)$ as a function of applied magnetic field ($B \parallel ab$ plane) and (f) polar intensity of A_g^6 for a magnetic field (7 T) applied parallel to the ab plane at two different crystal orientations. Sample temperature was 9 K (2 K) for $B \perp ab$ ($B \parallel ab$). Error bars represent standard errors from fitting function.
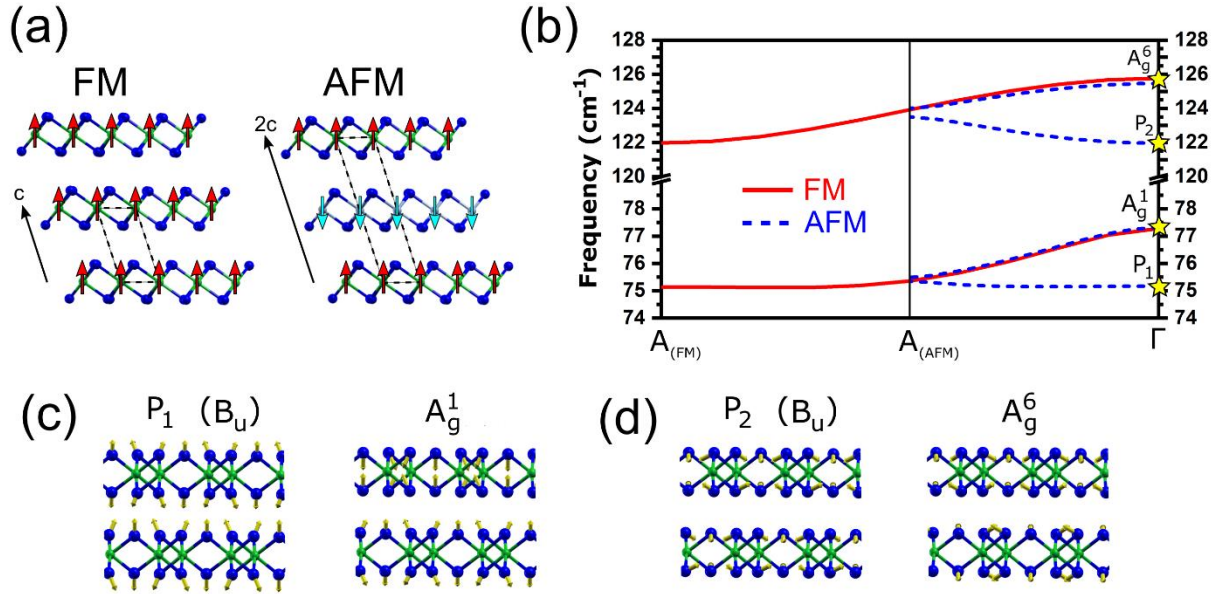
Figure 5: (a) Comparing the unit cell for the FM and AFM stacked structures, where the AFM unit cell is doubled in the *c*-direction. (b) Calculated phonon dispersion showing the Raman-active modes in the FM (red, solid) and AFM (blue, dashed) stacking in bulk CrI_3 in the monoclinic crystal structure. In the AFM case, the doubling of the unit cell along the *c*-direct in real space results in the $A_{(FM)}$-point folding into Γ, such that the number of modes is doubled compared to the FM case. The $\Gamma - A$ distance in the AFM case is half that of the FM case. Modes that correspond to P_1, A_g^1, P_2, and A_g^6 are highlighted and their atomic vibrations are shown in (c) and (d).

REFERENCES:

1   Gong, C. *et al.* Discovery of intrinsic ferromagnetism in two-dimensional van der Waals crystals. *Nature* **546**, 265-269 (2017).

2   Huang, B. *et al.* Layer-dependent ferromagnetism in a van der Waals crystal down to the monolayer limit. *Nature* **546**, 270-273 (2017).

3   Lee, J. U. *et al.* Ising-type magnetic ordering in atomically thin $FePS_3$. *Nano Lett.* **16**, 7433-7438 (2016).

4   Wang, X. Z. *et al.* Raman spectroscopy of atomically thin two-dimensional magnetic iron phosphorus trisulfide ($FePS_3$) crystals. *2D Mater.* **3**, 031009 (2016).

5   Shcherbakov, D. *et al.* Raman spectroscopy, photocatalytic degradation, and stabilization of atomically thin Chromium tri-iodide. *Nano Lett.* **18**, 4214-4219 (2018).

6   Bonilla, M. *et al.* Strong room-temperature ferromagnetism in VSe_2 monolayers on van der Waals substrates. *Nat. Nanotechnol.* **13**, 289-293 (2018).

7   Burch, K. S., Mandrus, D. & Park, J. G. Magnetism in two-dimensional van der Waals materials. *Nature* **563**, 47-52 (2018).

8   Huang, B. *et al.* Electrical control of 2D magnetism in bilayer CrI_3. *Nat. Nanotechnol.* **13**, 544-548 (2018).

9   Jiang, S. W., Li, L. Z., Wang, Z. F., Mak, K. F. & Shan, J. Controlling magnetism in 2D CrI_3 by electrostatic doping. *Nat. Nanotechnol.* **13**, 549-553 (2018).

10   Jiang, S. W., Shan, J. & Mak, K. F. Electric-field switching of two-dimensional van der Waals magnets. *Nat. Mater.* **17**, 406-410 (2018).

11   Li, T. *et al.* Pressure-controlled interlayer magnetism in atomically thin CrI_3. *Nat. Mater.* **18**, 1303-1308 (2019).

12   Wang, Z. *et al.* Very large tunneling magnetoresistance in layered magnetic semiconductor CrI_3. *Nat. Commun.* **9**, 2516 (2018).

13   Song, T. C. *et al.* Giant tunneling magnetoresistance in spin-filter van der Waals heterostructures. *Science* **360**, 1214-1218 (2018).

14   Kim, H. H. *et al.* One million percent tunnel magnetoresistance in a magnetic van der Waals heterostructure. *Nano Lett.* **18**, 4885-4890 (2018).

15   Kim, H. H. *et al.* Evolution of interlayer and intralayer magnetism in three atomically thin chromium trihalides. *P. Natl. Acad. Sci. USA* **116**, 11131-11136 (2019).

16   Li, Y. Y. *et al.* Giant anisotropic Raman response of encapsulated ultrathin black phosphorus by uniaxial strain. *Adv. Funct. Mater.* **27**, 1600986 (2017).

17   McCreary, A. *et al.* Intricate resonant Raman response in anisotropic ReS_2. *Nano Lett.* **17**, 5897-5907 (2017).

18   Zhang, K. N. *et al.* Raman signatures of inversion symmetry breaking and structural phase transition in type-II Weyl semimetal $MoTe_2$. *Nat. Commun.* **7**, 13552 (2016).

19   Tian, Y., Gray, M. J., Ji, H. W., Cava, R. J. & Burch, K. S. Magneto-elastic coupling in a potential ferromagnetic 2D atomic crystal. *2D Mater.* **3**, 025035 (2016).

20   McCreary, A. *et al.* Quasi-two-dimensional magnon identification in antiferromagnetic $FePS_3$ via magneto-Raman spectroscopy. *Phys. Rev. B* **101**, 064416 (2020).

21   Cenker, J. *et al.* Direct observation of 2D magnons in atomically thin CrI_3. (arXiv:2001.07025)

22   Li, S. *et al.* Magnetic field-induced quantum phase transitions in a van der Waals magnet. (arXiv:2001.09536)

23   Dean, C. R. *et al.* Boron nitride substrates for high-quality graphene electronics. *Nat. Nanotechnol.* **5**, 722-726 (2010).

24   Ponomarenko, L. A. *et al.* Tunable metal-insulator transition in double-layer graphene heterostructures. *Nat. Phys.* **7**, 958-961 (2011).

25   McGuire, M. A., Dixit, H., Cooper, V. R. & Sales, B. C. Coupling of crystal structure and magnetism in the layered, ferromagnetic insulator CrI_3. *Chem. Mater.* **27**, 612-620 (2015).

26   Klein, D. R. *et al.* Probing magnetism in 2D van der Waals crystalline insulators via electron tunneling. *Science* **360**, 1218-1222 (2018).

27   Sun, Z. *et al.* Giant nonreciprocal second-harmonic generation from antiferromagnetic bilayer CrI_3. *Nature* **572**, 497-501 (2019).

28   Sivadas, N., Okamoto, S., Xu, X. D., Fennie, C. J. & Xiao, D. Stacking-dependent magnetism in bilayer Cr_{I3}. *Nano Lett.* **18**, 7658-7664 (2018).

29   Jiang, P. H. *et al.* Stacking tunable interlayer magnetism in bilayer CrI_3. *Phys. Rev. B* **99**, 144401 (2019).

30   Soriano, D., Cardoso, C. & Fernandez-Rossier, J. Interplay between interlayer exchange and stacking in CrI_3 bilayers. *Solid State Commun.* **299**, 113662 (2019).

31   Jang, S. W., Jeong, M. Y., Yoon, H., Ryee, S. & Han, M. J. Microscopic understanding of magnetic interactions in bilayer CrI_3. *Phys. Rev. Mater.* **3**, 031001(R) (2019).

32   Ubrig, N. *et al.* Low-temperature monoclinic layer stacking in atomically thin CrI_3 crystals. *2D Mater.* **7**, 015007 (2019).

33   Larson, D. T. & Kaxiras, E. Raman spectrum of CrI_3: An *ab initio* study. *Phys. Rev. B* **98**, 085406 (2018).

34   Djurdjic-Mijin, S. *et al.* Lattice dynamics and phase transition in CrI_3 single crystals. *Phys. Rev. B* **98**, 104307 (2018).

35   Jin, W. C. *et al.* Raman fingerprint of two terahertz spin wave branches in a two-dimensional honeycomb Ising ferromagnet. *Nat. Commun.* **9**, 5122 (2018).

36   Chen, L. B. *et al.* Topological spin excitations in honeycomb ferromagnet CrI_3. *Phys. Rev. X* **8**, 041028 (2018).

37   Lee, I. *et al.* Fundamental spin interactions underlying the magnetic anisotropy in the Kitaev ferromagnet CrI3. *Phys. Rev. Lett.* **124**, 017201 (2020).

38   Seyler, K. *et al.* Ligand-field helical luminescence in a 2D ferromagnetic insulator. *Nat. Phys.* **14**, 277-281 (2018).

39   Chakraborty, B., Ramakrishna Matte, H. S. S., Sood, A. K., & Rao, C. N. R. Layer-dependent resonant Raman scattering of a few layer MoS_2. *J. Raman Spectr.* **44**, 92-96 (2013).

40   Berkdemir, A. *et al.* Identification of individual and few layers of WS_2 using Raman spectroscopy. *Sci. Rep.* **3**, 1755 (2013).

41   del Corro, E. *et al.* Excited excitonic states in 1L, 2L, 3L, and bulk WSe_2 observed by resonant Raman spectroscopy. *ACS Nano* **8**, 9629-9635 (2014).

42   Zhang, Y. *et al*. Magnetic order-induced polarization anomaly of Raman scattering in 2D magnet CrI_3. *Nano Lett*. **20**, 729-734 (2020).

43   Huang, B., Cenker, J., Zhang, X., Ray, E. L., Song, T., Taniguchi, T., Watanabe, K., McGuire, M. A., Xiao, D., & Xu, X. Tuning inelastic light scattering via symmetry control in the two-dimensional magnet CrI_3. *Nat. Nanotechnol.* **15**, 212-216 (2020).

44   Shcherbakov, D. *et al.* Raman spectroscopy, photocatalytic degradation, and stabilization of atomically thin Chromium tri-iodide. *Nano Lett.* **18**, 4214-4219 (2018).

45   Hohenberg, P. & Kohn, W. Inhomogeneous electron gas. *Phys. Rev. B* **136**, B864 (1964).

46   Kohn, W. & Sham, L. J. Self-consistent equations including exchange and correlation effects. *Phys. Rev.* **140**, A1133 (1965).

47   Giannozzi, P. *et al.* Advanced capabilities for materials modelling with QUANTUM ESPRESSO. *J. Phys.-Condens. Mater.* **29**, 465901 (2017).

48   Garrity, K. F., Bennett, J. W., Rabe, K. M. & Vanderbilt, D. Pseudopotentials for high-throughput DFT calculations. *Comp. Mater. Sci.* **81**, 446-452 (2014).

49   Vanderbilt, D. Soft self-consistent pseudopotentials in a generalized eigenvalue formalism. *Phys. Rev. B* **41**, 7892-7895 (1990).

50   Thonhauser, T. *et al.* Van der Waals density functional: Self-consistent potential and the nature of the van der Waals bond. *Phys. Rev. B* **76**, 125112 (2007).

51   Klimes, J., Bowler, D. R. & Michaelides, A. Chemical accuracy for the van der Waals density functional. *Journal of Phys.-Condens. Mat.* **22**, 022201 (2010).

52   Perdew, J. P. *et al.* Restoring the density-gradient expansion for exchange in solids and surfaces. *Phys. Rev. Lett.* **100**, 136406 (2008).

53   Togo, A. & Tanaka, I. First principles phonon calculations in materials science. *Scripta Mater.* **108**, 1-5 (2015).

54   Garrity, K. F. Combined cluster and atomic displacement expansion for solid solutions and magnetism. *Phys. Rev. B* **99**, 174108 (2019).

SUPPORTING INFORMATION

Distinct magneto-Raman signatures of spin-flip phase transitions in CrI$_3$

Amber McCreary,[1] Thuc T. Mai,[1,2] Franz G. Utermohlen,[2] Jeffrey R. Simpson,[1,3] Kevin F. Garrity,[4] Xiaozhou Feng,[2] Dmitry Shcherbakov,[2] Yanglin Zhu,[5] Jin Hu,[6] Daniel Weber,[7,⊥] Kenji Watanabe,[8] Takashi Taniguchi,[8] Joshua E. Goldberger,[7] Zhiqiang Mao,[5] Chun Ning Lau,[2] Yuanming Lu,[2] Nandini Trivedi,[2] Rolando Valdés Aguilar,[2,§] and Angela R. Hight Walker[1,*]

[1]Nanoscale Device Characterization Division, Physical Measurement Laboratory, National Institute of Standards and Technology, Gaithersburg, Maryland 20899, USA

[2]Department of Physics, The Ohio State University, Columbus, OH 43210, USA

[3]Department of Physics, Astronomy, and Geosciences, Towson University, Towson, MD 21252, USA

[4]Materials Measurement Science Division, Material Measurement Laboratory, National Institute of Standards and Technology, Gaithersburg, Maryland 20899, USA

[5]Department of Physics, The Pennsylvania State University, University Park, PA 16802, USA

[6]Department of Physics, University of Arkansas, Fayetteville, AR 72701, USA

[7]Department of Chemistry and Biochemistry, The Ohio State University, Columbus, OH 43210, USA

[8]National Institute for Materials Science, 1-1 Namiki Tsukuba Ibaraki 305-0044, Japan

⊥Current address: Battery and Electrochemistry Laboratory, Institute of Nanotechnology, Karlsruhe Institute of Technology, 76344 Eggenstein-Leopoldshafen, Germany

*Email: angela.hightwalker@nist.gov

§Email: valdesaguilar.1@osu.edu

Figure S1: (a) Schematic showing top view of the crystal structure of a monolayer of CrI_3. (b,c) Comparing between the (b) rhombohedral and (c) monoclinic stacking of two layers of CrI_3, where the rhombohedral (monoclinic) results in ferromagnetic (antiferromagnetic) spin stacking.
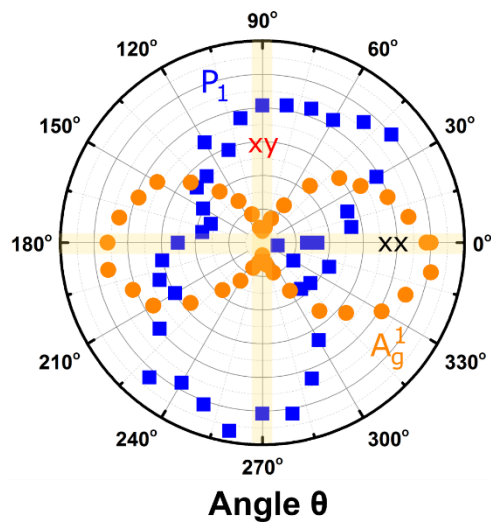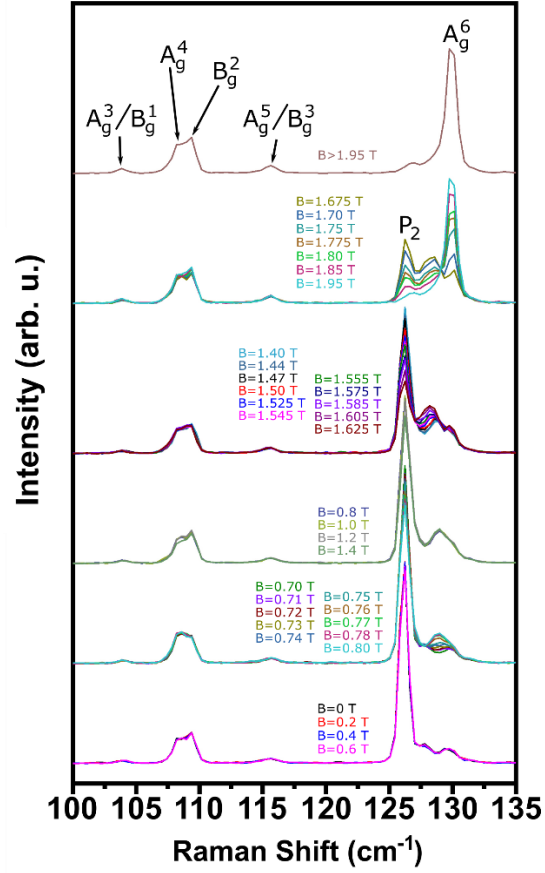

Figure S2: Polar intensity plot as a function of θ for P_1 mode and nearby A_g^1 phonon at T = 5 K and B = 0 T.

Frequency (cm^{-1})	Symmetry	Vibration
51.09	B_g	
52.15	A_g	
77.00	A_g	
87.92	B_g	
100.99	A_g	
101.22	B_g	
Continued…		
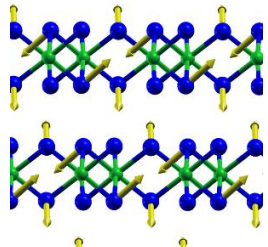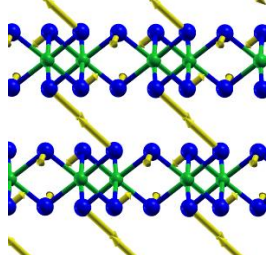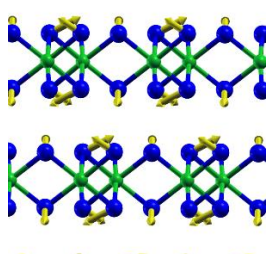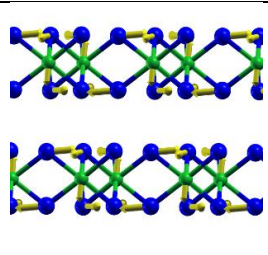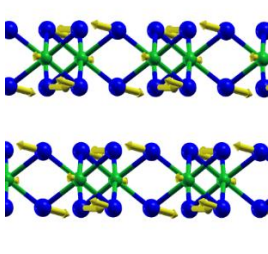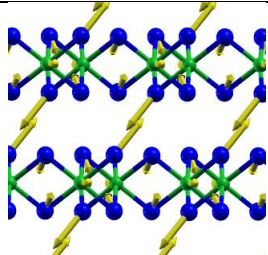
102.54	B_g	
103.77	A_g	
125.94	A_g	
202.74	B_g	
226.30	A_g	
227.93	B_g	

Table S1: DFT-calculated Raman-active phonons in monoclinic, bulk CrI$_3$.

Figure S3: Raman spectra of 10 L CrI$_3$ as a function of magnetic field (applied perpendicular to the *ab* plane) at T = 9 K, showing a larger frequency range compared with Figure 3 of the main text where negligible changes are observed in the other phonon modes A_g^3/B_g^1, A_g^4, B_g^2, and A_g^5/B_g^3.
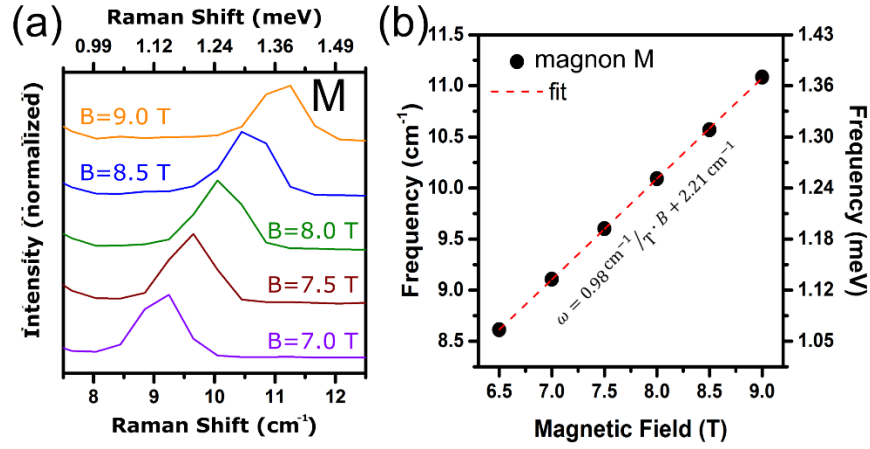
Figure S4: (a) Low-frequency Raman spectra at T = 5 K showing the true FM resonance (FMR), *i.e.* magnon, in CrI_3 that blueshifts with increasing magnetic field. At lower field values, we are unable to observe the FMR since it is below our spectrometer cutoff (~ 7 cm^{-1}). From the fit in (b), we extract $g \approx 2.08 \pm 0.05$ and $\omega_{B=0T} = 2.21 \pm 0.3$ cm^{-1} (0.27 ± 0.04 meV).
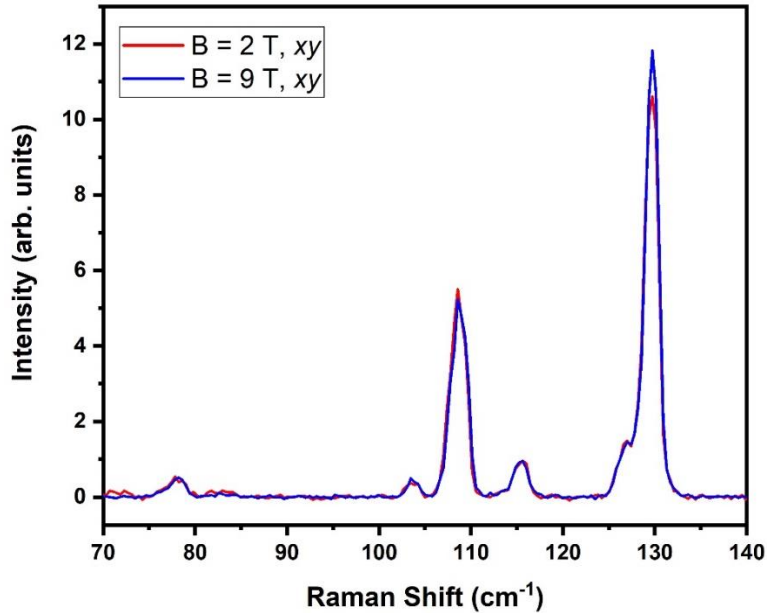
Figure S5: Comparing the Raman spectra (T = 9 K) of 10 L CrI_3 at B = 2 T and 9 T, where the magnetic field is applied perpendicular to the *ab* plane (*i.e.* parallel/antiparallel to the direction of the spins). Negligible changes are observed between the two spectra.
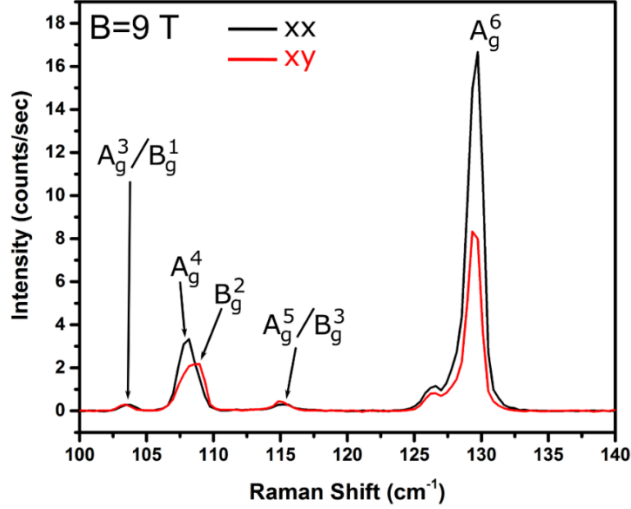
Figure S6: Comparing Raman spectra at B = 9 T (B ⊥ *ab*) and T = 9 K in the parallel (*xx*, black) and cross (*xy*, red) polarization configurations. Since we still observe a splitting in the mode at ≈108 cm⁻¹, as opposed to one degenerate mode, we deduce the thin CrI₃ is still in the monoclinic phase after the magnetic phase transition from AFM to FM interlayer stacking.
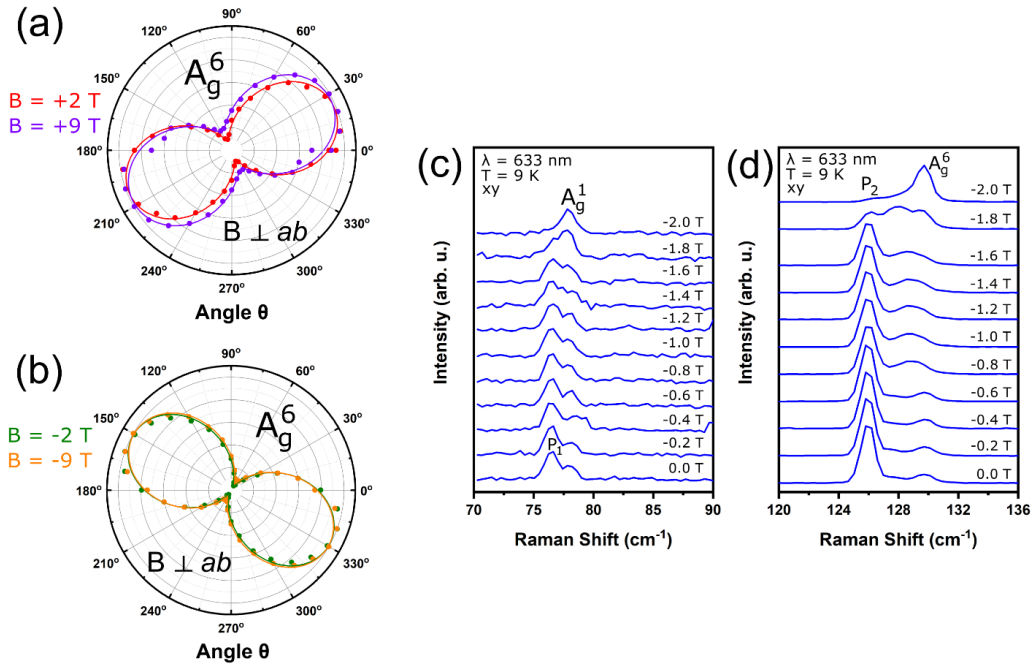
Figure S7: Comparing polar intensity plots for A_g^6 for (a) B = +2 T and +9 T and (b) B = -2 T and -9 T at 9 K, with the magnetic field applied perpendicular to the *ab* plane. Frequency range showing (c) P_1, A_g^1 and (d) P_2, A_g^6 as a function of applied negative magnetic field (B ⊥ *ab*), showing the same trend as applied positive magnetic fields.

Temperature Dependence of Magnetic Phase Transition
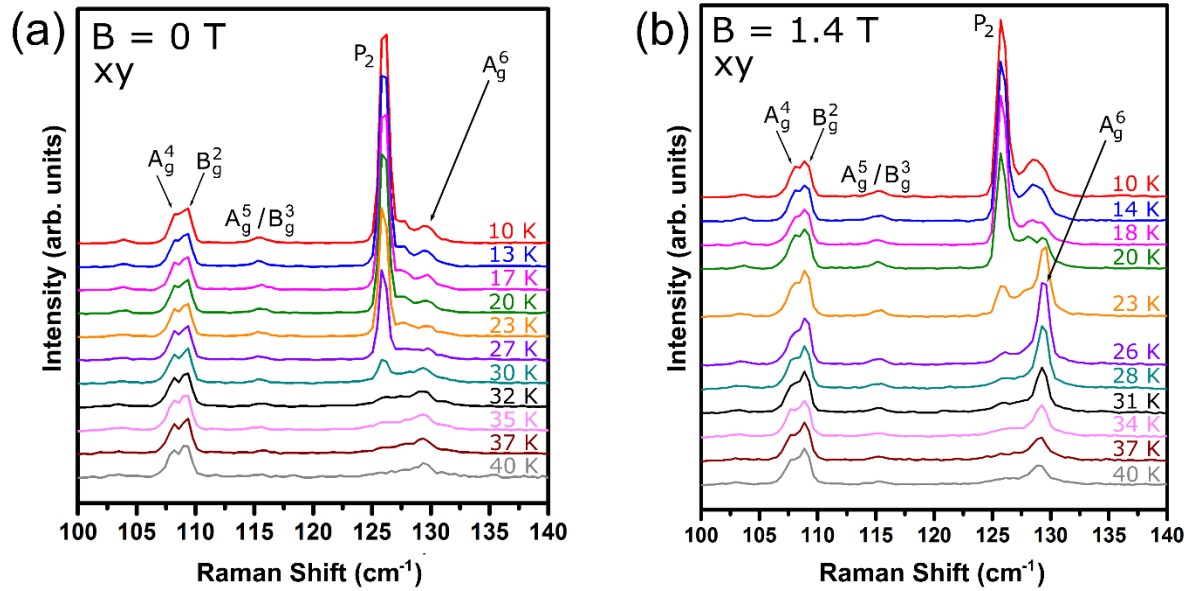
Figure S8: (a) Temperature dependence of the Raman spectra at B = 0 T in *xy* polarization configuration, where P$_2$ disappears above 32 K and the A_g^6 mode remains small. (b) Temperature dependence at B = 1.4 T, where increasing the temperature results in a similar evolution of the Raman spectra as further application of magnetic field, including the appearance/increased intensity of A_g^6, until it disappears again as the sample is warmed (B ⊥ *ab*).

      Figures S8a and S8b demonstrate that increasing temperature can have the same effect as increasing magnetic field to complete the phase transition in thin CrI$_3$. Figure S8a shows the evolution of the Raman spectra at B = 0 T, in *xy* configuration, as a function of temperature. As the temperature of the CrI$_3$ is increased, the intensity of P_2 decreases until it is unobservable above T = 35 K. In this case, with no magnetic field applied, the intensity of A_g^6 remains small, as expected. On the contrary, when a magnetic field slightly below B_c is applied, such as B = 1.4 T in Figure S8b, increasing the temperature can be used in the same fashion as increasing the magnetic field to push CrI$_3$ through the phase transition, as was shown in magneto-resistance as well.[1] In this case, increasing the temperature by ≈16 K is enough to drive the phase transition that would have required an extra ≈0.6 T of magnetic field. With the magnetic field applied, the intensity of A_g^6 increases with increasing temperature, but as the temperature increases further towards the Curie temperature, A_g^6 starts to disappear again, confirming that the phase transition we are observing is magnetic in nature.

*In Figure S8b, the sample was zero field-cooled to T = 10 K, where a magnetic field of 1.4 T was applied perpendicular to the *ab* plane. Keeping the field at 1.4 T, the temperature was then increased to the values shown in the graph.
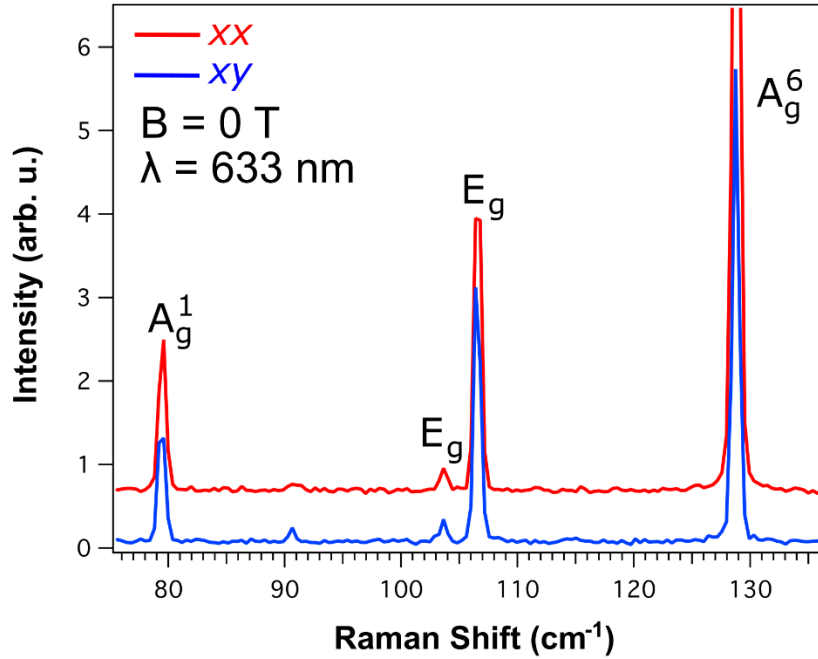
Figure S9: Raman spectra for bulk ($\approx$1 mm thickness, not encapsulated in hBN) CrI_3 at T = 5 K (B $\perp$ *ab*). The phonons are labeled using the rhombohedral point group $3\bar{R}$, since bulk CrI_3 does undergo a phase transition from monoclinic to rhombohedral at $\approx$200 K. Modes P_1 and P_2 were not observed, and in agreement with the rhombohedral structure, the mode at $\approx$107 cm^{-1} is degenerate in *xx* and *xy* polarization configurations.
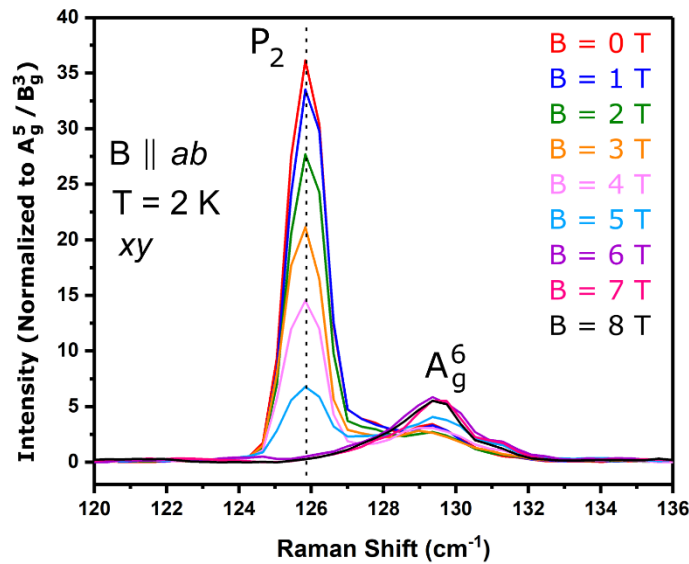

Figure S10: Evolution of P_2 and A_g^6 as a function of applied magnetic field when the field is applied parallel to the *ab* plane. Unlike the case of B $\perp$ *ab*, a continuous decrease of P_2 as a function of field is observed. No frequency shift of P_2 is seen.
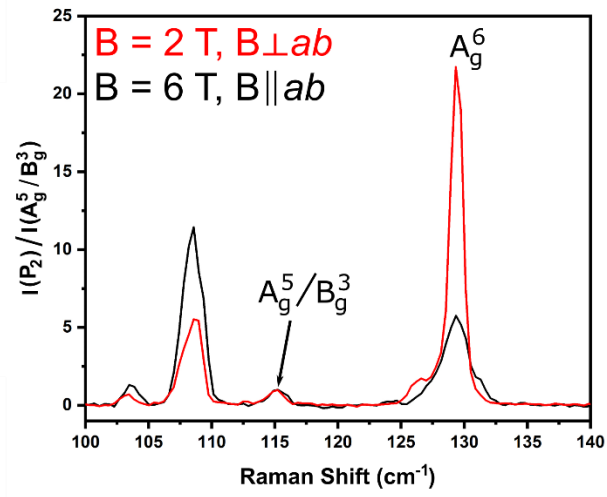
Figure S11: Comparing the Raman spectra (T = 9 K) above the magnetic-field driven spin-flip phase transition when the magnetic field is applied perpendicular (red) and parallel (black) to the *ab* plane.

P_1 and P_2 as Zone-Folded Phonons:

DFT Calculated Phonon Frequencies
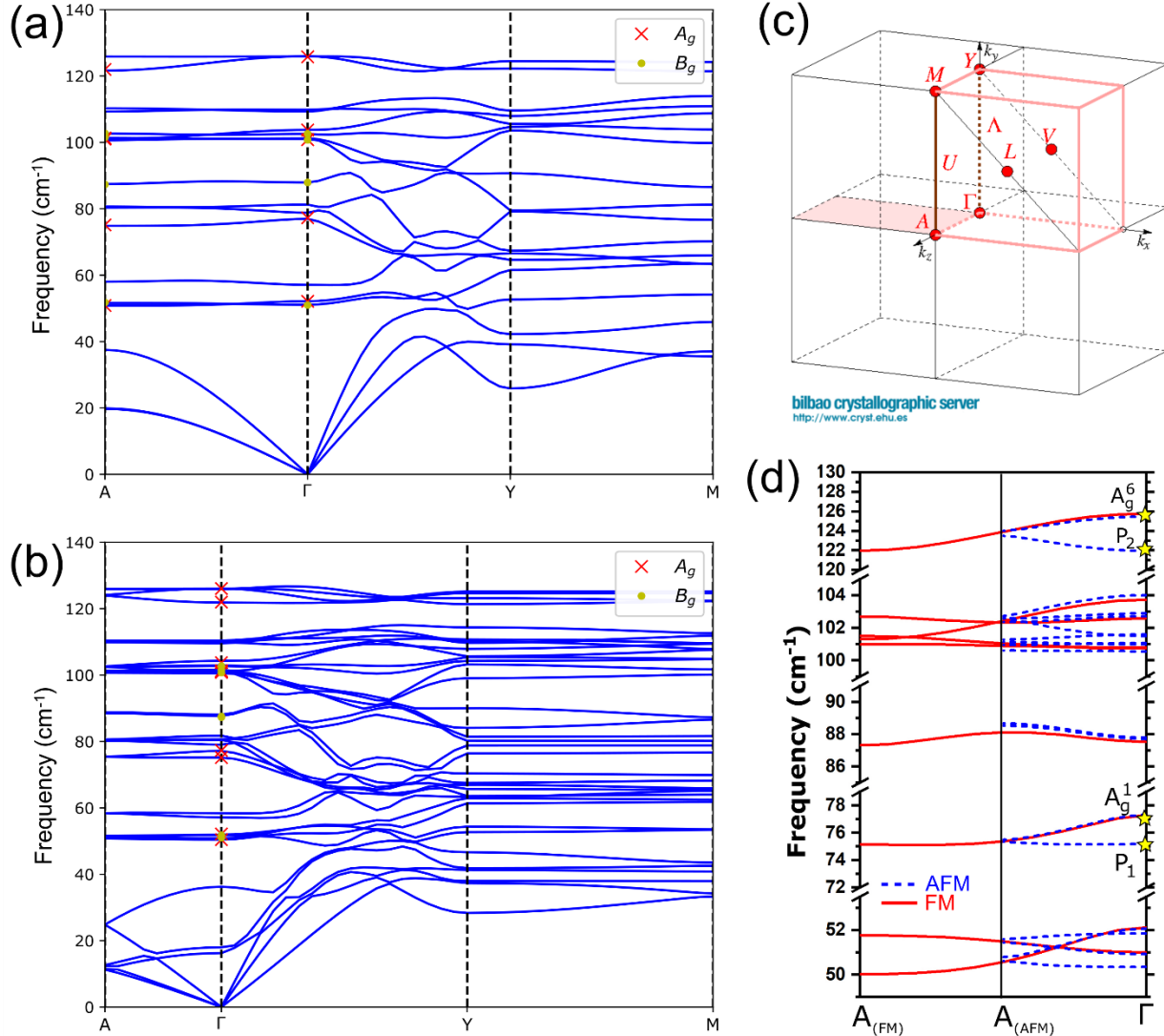
Figure S12: Calculated phonon dispersion of (a) FM and (b) AFM stacking for bulk CrI_3 in the monoclinic crystal structure. The relevant Brillouin zone from Bilbao crystallographic server[2-4] is shown in (c). In the AFM case, the unit cell doubles along the c-direction in real space, such that the A-point folds into Γ and the number of modes is doubled compared to the FM case. The symmetry of the Raman-active modes is marked on the phonon dispersion as A_g or B_g at the Γ point. It should be noted that a constant number of points was used between the high symmetry k-points for both the FM and AFM cases even though the size of the Brillouin zone in the $\Gamma - A$ direction is half in the AFM vs. FM cases. Thus, it is not possible to visually compare the derivatives of the acoustic modes at Γ in order to get the speed of sound. (d) Comparing the calculated phonon dispersion showing the Raman-active modes between 45 cm^{-1} and 130 cm^{-1} in the FM (red, solid) and AFM (blue, dashed) stacking configurations. The $\Gamma - A$ distance in the AFM case is half that of the FM case.

Ferromagnetic (FM)		Antiferromagnetic (AFM)		
Frequency	Q-Point	Frequency	Q-Point	Character
50.02	A	50.35	Γ	oo-phase
51.00	Γ	50.93	Γ	in-phase
51.77	A	51.85	Γ	oo-phase
52.12	Γ	52.07	Γ	in-phase
75.15	A	75.17	Γ	oo-phase
77.28	Γ	77.32	Γ	in-phase
87.31	A	87.70	Γ	oo-phase
87.53	Γ	87.80	Γ	in-phase
100.80	Γ	100.57	Γ	in-phase
100.73	Γ	100.98	Γ	in-phase
100.98	A	101.07	Γ	oo-phase
101.32	A	101.49	Γ	oo-phase
101.51	A	101.60	Γ	oo-phase
102.59	Γ	102.73	Γ	mix-phase
102.70	A	102.90	Γ	mix-phase
103.74	Γ	104.02	Γ	in-phase
121.98	A	121.96	Γ	oo-phase
125.77	Γ	125.47	Γ	in-phase
202.06	Γ	202.55	Γ	in-phase
201.87	A	202.67	Γ	oo-phase
225.54	A	226.31	Γ	oo-phase
226.36	Γ	226.70	Γ	in-phase
226.79	A	227.14	Γ	oo-phase
226.87	Γ	227.47	Γ	in-phase

Table S2: DFT-calculated phonon frequency and Q-points for the Raman-active phonons in monoclinically-stacked, bulk CrI_3 for ferromagnetic (FM) and antiferromagnetic (AFM) interlayer exchange coupling. For FM exchange, we list the phonon frequencies and symmetries at the A-point in the Brillouin zone as well, which is along the c-direction in real space. In the AFM state, the unit cell doubles and the A-point is folded into Γ and thus can become Raman-active. In general, the splitting between the mode originally at Γ and the mode zone-folded from the A-point are very small and most likely not resolvable. However, for the pairs of modes highlighted in red, the splitting is significant, with the mode from A at a lower frequency than the one from Γ.

Frequency (cm⁻¹)	Q-Point in FM	Symmetry	Vibration
75.2	A	B_u	
77.3	Γ	A_g	
122.0	A	B_u	
125.8	Γ	A_g	

Figure S13: DFT-calculated phonon vibrations for A_g^1 and A_g^6 as well as the zone-folded phonons at lower frequency. Eigenvectors are calculated for a bulk system, but are pictured as a bilayer system. Looking at the vibrations for a bilayer system, the two zone-folded vibrations would have B_u symmetry with the inversion center in-between the two layers. When magnetic ordering is considered, however, where the two layers have AFM stacking, there is no longer inversion symmetry and the modes will be of B symmetry, and thus can be Raman active.

P_1 and P_2 as Bound Two-Magnon Excitations:

We considered the possibility that P_1 and P_2 could be intralayer bound two-magnon excitations with a total spin of zero, given that they do not shift with B field. A two-excitation consists of one magnon propagating in the $+k$ direction and other magnon propagating in the $-k$, such that $+k - k = 0$ and conservation of momentum is conserved, allowing these excitiations to be seen in Raman spectroscopy. If the bound two-magnon excitation had a total spin of zero, then the excitation would not be expected to shift in magnetic field, as was experimentally observed for $P_{1,2}$. In ferromagnetic systems, two-magnon excitations are expected to naturally arise from bond-dependent interactions like the Kitaev interaction,[5] which a recent experiment[6] suggests is the dominant interaction of CrI_3. We can see how the Kitaev interaction can produce two-magnon excitations by expressing the Kitaev interaction in the Holstein-Primakoff representation, which yields terms of the form $a_k^\dagger a_{-k}^\dagger$, corresponding to the creation of a pair of magnons with opposite momenta.

We performed an exact diagonalization calculation of the two-magnon density of states (DOS) and Raman intensity at zero temperature for a spin-3/2 system of 6-sites (a single honeycomb plaquette) described by the $JK\Gamma$ Hamiltonian

$$\hat{H}_{JK\Gamma} = \sum_{\langle r,r'\rangle \in \alpha\beta(\gamma)} \left[J\boldsymbol{S}_r \cdot \boldsymbol{S}_{r'} + K S_r^\gamma S_{r'}^\gamma + \Gamma \left(S_r^\alpha S_{r'}^\beta + S_r^\beta S_{r'}^\alpha \right) \right]$$

which is the most general nearest-neighbor spin-spin interaction Hamiltonian allowed by the symmetries of a CrI_3 monolayer, where $\gamma \in \{x, y, z\}$ labels the bond type through which the neighboring Cr ions at r, r' are interacting, α, β label the other two bond types, J is the Heisenberg coupling, K is the Kitaev coupling, and Γ is the symmetric off-diagonal coupling. Using the values of the coupling constants obtained by Lee et $al.$,[25] namely $J = -0.212$ meV, $K = -5.190$ meV, and $\Gamma = -0.068$ meV, we found that the entire two-magnon DOS and Raman spectrum (see Figure S12) shift with applied B field, thereby ruling out this potential mechanism for P_1 and P_2.
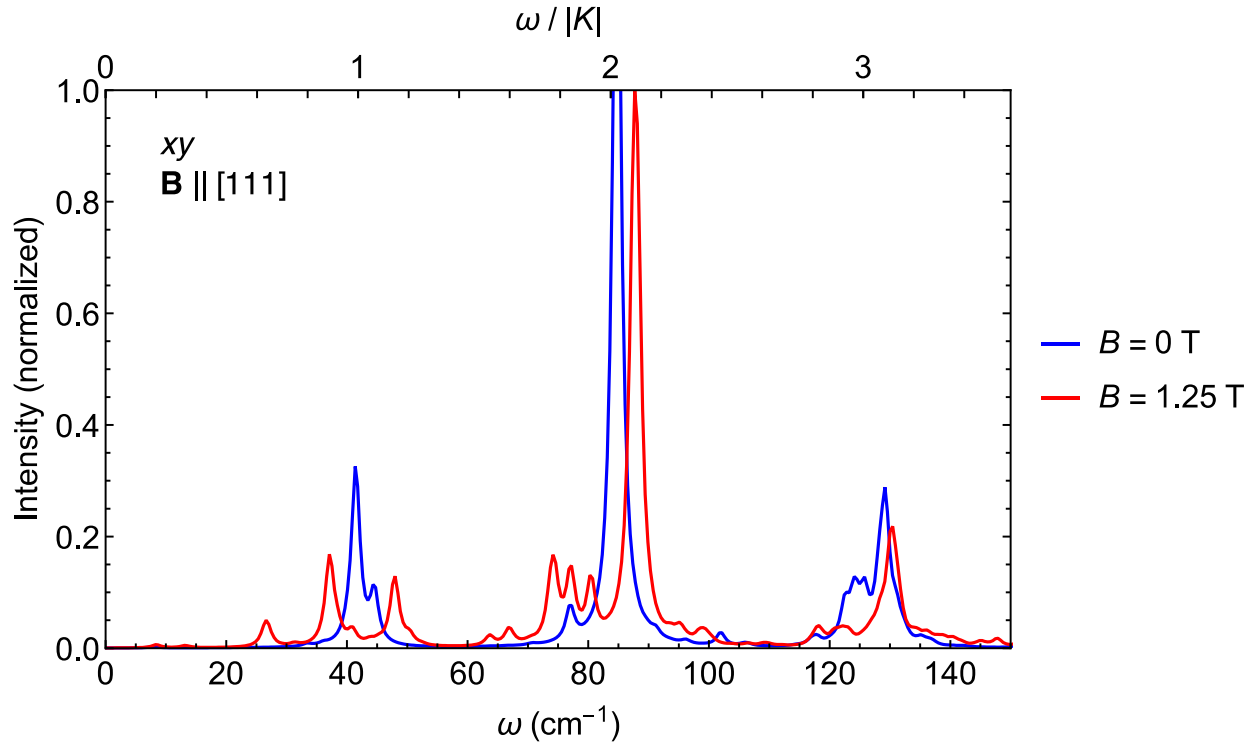
Figure S14: Exact diagonalization calculation of the zero-temperature Raman spectra in the cross (*xy*) polarization configuration for a spin-3/2 system of 6-sites (a single honeycomb plaquette) described by the *JK*Γ Hamiltonian and using the values of the coupling constants obtained by Lee *et al.*[25] This calculation serves as an estimate of the Raman behavior of monolayer CrI$_3$. When a *B* field is applied out of the plane, the entire Raman spectrum shifts.

P_1 and P_2 as Bound Magnon-Phonon Pairs:

Another theoretical model we considered was that if the spins in CrI$_3$ were oriented in-plane and antiferromagnetically stacked, as has been reported in CrCl$_3$,[7] P_1 and P_2 could correspond to the bound state of a phonon and a magnon, where the phonon would be at a slightly higher frequency (A_g^1 for P_1, and A_g^6 for P_2) and the magnon would be a soft magnon $\gamma_{(0,0,\pi),+}$. We considered this as an option because the magnon (and hence the phonon-magnon bound state) carries B_g representation of the $2'/m$ magnetic group in our 10-layer sample and exhibits the highest intensity in cross polarization, as was observed for $P_{1,2}$. The associated magnetic group $2'/m$ generated by magnetic rotation C'_{2x} and mirror M_x for the spins oriented in the *ab* plane is also consistent with the angle-dependence of second harmonic generation (SHG) signals observed by Z. Sun *et al.*,[8] since mirror M_x and 2-fold rotation C_{2x} enforces similar constrains to nonlinear susceptibility with respect to in-plane polarization. When the perpendicular magnetic field B_z exceeds the critical value of 2 T, the in-plane order AFM_x could be destabilized and transitioned into out-of-plane ferromagnetism FM_z at larger fields.

We use the isotropic Heisenberg interaction between nearest neighbors as a minimal model in order to extract the symmetry properties of the magnon modes. The acquired representation of magnon modes and selection rules from Raman scattering are expected to be universal, insensitive to the exact form of the Hamiltonian. However, the frequency of the magnon modes can be an artifact of such toy models and should not be compared directly with experiments.

We label the lattice sites of the layered honeycomb lattice by

$$\boldsymbol{R} = \boldsymbol{r} + z\vec{a}_3 \equiv (r_1, r_2, z, s), \quad s = A/B \text{ labeling two sublattices} \tag{1}$$

$$\boldsymbol{r} \equiv r_1 \vec{a}_1 + r_2 \vec{a}_2 + \vec{R}_s, \quad r_{1,2}, z \in \mathbb{Z} \tag{2}$$

where $\{\vec{a}_i | i = 1,2,3\}$ are the primitive lattice vectors, and $\boldsymbol{r}$ is the in-plane 2D coordinate.

The monoclinic space group $2/m$ is generated by the following point group symmetries:

$$(x, y, z) \xrightarrow{M_x} (-x, y, z) \tag{3}$$

$$(x, y, z) \xrightarrow{C_{2x}} (x, -y, -z) \tag{4}$$

and their combination is the inversion symmetry.

The following minimal model of spin-3/2's is considered:

$$\hat{H} = -J \sum_{\langle r,r' \rangle, z} S_{r,z} \cdot S_{r',z} + J_z \sum_{r,z} S_{r,z} \cdot S_{r,z+1} - B_z \sum_R S_R^z \tag{5}$$

where $J \gg J_z, B_z > 0$ are all positive parameters.

I.   LARGE FIELD CASE: OUT-OF-PLANE FERROMAGNETISM

For ferromagnetism (FM) along $\hat{z}$-axis (coined FM_z), we use the following Holstein-Primakoff representation to derive the spin wave theory:

$$S_R^z = S - a_R^\dagger a_R, \qquad S_R^+ = S_R^x + iS_R^y = \sqrt{2S - a_R^\dagger a_R} \cdot a_R \tag{6}$$

In this FM_z phase, the unbroken magnetic symmetries (magnetic point group $2'/m'$) are

$$M_x' \equiv M_x \cdot \mathrm{T}, \quad C_{2x}' \equiv C_{2x} \cdot \mathrm{T} \tag{7}$$

where T is the time-reversal operator. The magnon operator transforms under them as

$$a_R \overset{M_x'}{\rightarrow} -a_{M_x R}, \quad a_R \overset{C_{2x}'}{\rightarrow} -a_{C_{2x} R}, \tag{8}$$

The associated linear spin wave Hamiltonian reads

$$\hat{H}_{FM_z} = (3JS + B_z - 2J_z S) \sum_R a_R^\dagger a_R - JS \sum_{\langle r,r' \rangle, z} a_{r,z}^\dagger a_{r',z} + J_z S \sum_{r,z} a_{r,z}^\dagger a_{r,z+1} + h.c. \tag{9}$$

It's straightforward to obtain the two magnon branches with frequency:

$$\omega_{k,k_z,\pm} = JS(3 \mp |f_k|) + B_z - 2J_z S(1 - \cos k_z) \tag{10}$$

where $\boldsymbol{k}$ labels the in-plane 2D momentum. $f_k = \sum_{j=1,2,3} e^{i\boldsymbol{k} \cdot \vec{\delta}_j}$ is the structure factor of honeycomb nearest neighbors as in graphene, satisfying $f_{\boldsymbol{k}=(0,0)} = 3$. The wavefunction of the two magnon modes are given by

$$\gamma_{k,\pm} \equiv \left(a_{k,A} \pm a_{k,B} \right)/\sqrt{2} \tag{11}$$

It is straightforward to check how they transform under symmetries:

$$\gamma_{k,\pm} \overset{M_x'}{\rightarrow} \mp \gamma_{-M_x k,\pm}, \qquad \gamma_{k,\pm} \overset{C_{2x}'}{\rightarrow} -\gamma_{-C_{2x} k,\pm} \tag{12}$$

since M_x switches two sublattices but not C_{2x}. For magnons at the zone center Γ, the soft $\gamma_{\Gamma,+}$ mode is odd under both symmetries and belongs to B_g representation of point group $2/m$. On the other hand, the high frequency $\gamma_{\Gamma,-}$ mode is odd under inversion symmetry and hence not Raman active. This explains

why experiments only observe the soft B_g mode $\gamma_{\Gamma,+}$ mode above $B_z \geq 7$ T, but not the high frequency mode $\gamma_{\Gamma,-}$.

II. SMALL FIELD CASE: IN-PLANE ANTIFERROMAGNETISM

As suggested by the observation of SHG in bilayer CrI₃,[7] multilayer CrI₃ is likely to exhibit antiferromagnetism (AFM) between two neighboring layers. In the limit of a small magnetic field $B_z < 2$ T, we consider an in-plane moment along the $\hat{x}$-axis as reported in CrCl₃.[23] The Holstein-Primakoff representation writes:

$$S_{\bm{R}}^x = (-1)^z \cdot \left(S - a_{\bm{R}}^\dagger a_{\bm{R}}\right), \quad S_{\bm{R}}^{(-1)^z} \equiv S_{\bm{R}}^x + (-1)^z \mathrm{i} S_{\bm{R}}^z = \sqrt{2S - a_{\bm{R}}^\dagger a_{\bm{R}}} \cdot a_{\bm{R}} \tag{13}$$

For an even number of layers $L_z = 0 \bmod 2$, the magnetic point group is $2'/m$ generated by C'_{2x} and M_x. The boson operator transforms as

$$a_{\bm{R}} \xrightarrow{M_x} -a_{M_x \bm{R}}, \quad a_{\bm{R}} \xrightarrow{C'_{2x}} a_{C_{2x}\bm{R}} \tag{14}$$

The linear spin wave Hamiltonian writes

$$\hat{H}_{AFM_x} = \sum_{\bm{R}} (3JS + 2J_z S) a_{\bm{R}}^\dagger a_{\bm{R}} - JS \sum_{\langle r,r'\rangle,z} a_{r,z}^\dagger a_{r',z} + J_z S \sum_{r,z} a_{r,z}^\dagger a_{r,z+1}^\dagger + h.c.$$
$$- \mathrm{i} B_z \sqrt{2S} \sum_{\bm{R}} (-1)^z \left(a_{\bm{R}}^\dagger - a_{\bm{R}}\right) \tag{15}$$

Four branches of magnons are obtained with frequency:

$$\Omega_{\bm{k},k_z,\pm} = \sqrt{\omega_{\bm{k},\pm}\left(\omega_{\bm{k},\pm} + 4J_z S\right) + (2J_z S \sin k_z)^2} \tag{16}$$

where $\omega_{\bm{k},\pm} \equiv JS(3 \mp |f_k|)$ is the FM magnon dispersion within each 2D honeycomb plane. In particular, the magnon dispersion is not affected by the out-of-plane magnetic field B_z. It would, however, be affected by an in-plane magnetic field $B_{x,y}$, which is not consistent with our experimental observations for P_1 and P_2

There are two soft magnon modes, $\gamma_{(0,0,0),+}$ and $\gamma_{(0,0,\pi),+}$. Their symmetry characters are summarized in Table S3. They belong to A_u and B_g representations of group $2/m$, and the B_g mode $\gamma_{(0,0,\pi),+}$ is the only Raman active branch of soft magnons.

If the number of layers is odd, the crystal symmetry $2/m$ is fully preserved. Under symmetry operations, the bosons transform as

$$a_{\boldsymbol{R}} \overset{M_x}{\rightarrow} -a_{M_x \boldsymbol{R}}, \qquad a_{\boldsymbol{R}} \overset{C_{2x}}{\rightarrow} a_{C_{2x} \boldsymbol{R}} \tag{17}$$

The associated symmetry representations of magnons are summarized in Table S4. In this case, both soft magnons are Raman active and belong to B_g representation.

Modes	M_x'	C_{2x}'	Irrep.	Raman active?
$\gamma_{k_z=0,+}$	-	+	A_u	No
$\gamma_{\pi,+}$	-	-	B_g	Yes
$\gamma_{k_z=0,-}$	+	+	A_g	Yes
$\gamma_{\pi,-}$	+	-	B_u	No

Table S3. Symmetry characters (magnetic point group $2'/m$) of magnons in the AFM_x phase, in a thin film of CrI$_3$ with an even number of layers.

Modes	M_x	C_{2x}	Irrep.	Raman active?
$\gamma_{k_z=0,+}$	-	-	B_g	Yes
$\gamma_{\pi,+}$	-	-	B_g	Yes
$\gamma_{k_z=0,-}$	+	-	B_u	No
$\gamma_{\pi,-}$	+	-	B_u	No

Table S4. Symmetry characters (magnetic point group $2/m$) of magnons in the AFM_x phase, in a thin film of CrI$_3$ with an odd number of layers.

III.   SMALL FIELD CASE: OUT-OF-PLANE ANTIFERROMAGNETISM

Finally, we consider out-of-plane AFM order AFM_z as a comparison to AFM_x. The calculation is straightforward and one can show its magnon spectra as

$$\Omega_{\boldsymbol{k},k_z,\pm,\eta_z=\pm 1} = \left| B_z + \eta_z \sqrt{\omega_{\boldsymbol{k},\pm}(\omega_{\boldsymbol{k},\pm} + 4J_z S) + (2J_z S \sin k_z)^2} \right| \tag{18}$$

Clearly, all magnon frequencies shift with the applied magnetic field B_z, which is not consistent with our data for P_1 and P_2.

For comparison, we also list the representations of magnon modes at zone center Γ, for the case of even (Table S5) vs. odd (Table S6) layers in the thin film. They are the same as in the AFM_x phase, although their magnetic point groups are different from the AFM_x phase.

Modes	M'_x	C_{2x}	Irrep.	Raman active?
$\gamma_{k_z=0,+}$	-	+	A_u	No
$\gamma_{\pi,+}$	-	-	B_g	Yes
$\gamma_{k_z=0,-}$	+	+	A_g	Yes
$\gamma_{\pi,-}$	+	-	B_u	No

Table S5. Symmetry characters (magnetic point group $2/m'$) of magnons in the AFM_z phase, in a thin film of CrI$_3$ with an even number of layers.

Modes	M'_x	C'_{2x}	Irrep.	Raman active?
$\gamma_{k_z=0,+}$	-	-	B_g	Yes
$\gamma_{\pi,+}$	-	-	B_g	Yes
$\gamma_{k_z=0,-}$	+	-	B_u	No
$\gamma_{\pi,-}$	+	-	B_u	No

Table S6. Symmetry characters (magnetic point group $2'/m'$) of magnons in the AFM_z phase, in a thin film of CrI$_3$ with an odd number of layers.

In summary, if $P_{1,2}$ were due to the bound state of a magnon and a phonon where the spins were aligned in-plane, they would not be expected to shift in frequency under the application of a magnetic field perpendicular to the *ab* plane, which follows the observed behavior of $P_{1,2}$. They would, however, be expected to display a shift in frequency when the magnetic field was applied in the *ab* plane, but this is not consistent with what was observed in Figure S10. Thus, we have ruled out that $P_{1,2}$ are due to the bound state of a magnon and a phonon.

REFERENCES:

1   Wang, Z. *et al.* Very large tunneling magnetoresistance in layered magnetic semiconductor CrI_3. *Nat. Commun.* **9**, 2516 (2018).

2   Aroyo, M. I. *et al.* Crystallography online: Bilbao Crystallographic Server. *Bulgarian Chemical Communications* **43**, 183-197 (2011).

3   Aroyo, M. I. *et al.* Bilbao crystallographic server: I. Databases and crystallographic computing programs. *Zeitschrift Fur Kristallographie* **221**, 15-27 (2006).

4   Aroyo, M. I., Kirov, A., Capillas, C., Perez-Mato, J. M. & Wondratschek, H. Bilbao crystallographic server. II. Representations of crystallographic point groups and space groups. *Acta Crystallographica a-Foundation and Advances* **62**, 115-128 (2006).

5   Pradhan, S., Patel, N. D. & Trivedi, N.   (arXiv:1908.10877).

6   Lee, I. *et al.* Fundamental spin interactions underlying the magnetic anisotropy in the Kitaev ferromagnet CrI_3. *Phys. Rev. Lett*. **124**, 017201 (2020)

7   Klein, D. R. *et al.* Enhancement of interlayer exchange in an ultrathin two-dimensional magnet. *Nat. Phys.* (2019).

8   Sun, Z. *et al.* Giant nonreciprocal second-harmonic generation from antiferromagnetic bilayer CrI_3. *Nature* **572**, 497-501 (2019).